

# Deep-Subwavelength Holey Acoustic Second-Order Topological Insulators

Zhiwang Zhang, Houyou Long, Chen Liu, Chen Shao, Ying Cheng,\* Xiaojun Liu,\* and Johan Christensen\*

Higher-order topological insulators (HOTIs) belong to a new class of materials with unusual topological phases. They have garnered considerable attention due to their capabilities in confining energy at the hinges and corners, which is entirely protected by the topology, and have thus become attractive structures for acoustic wave studies and control. However, for most practical applications at audible and low frequencies, compact and subwavelength implementations are desirable in addition to providing robust guiding of sound beyond a single-frequency operation. Here, a holey HOTI capable of sustaining deeply confined corner states 50 times smaller than the wavelength is proposed. A remarkable resilience of these surface-confined acoustic states against defects is experimentally observed, and topologically protected sound is demonstrated in three different frequency regimes. Concerning this matter, the findings will thus have the capability to push forward exciting applications for robust acoustic imaging way beyond the diffraction limit.

The discovery of topological insulators (TIs)<sup>[1,2]</sup> and the strikingly robust transmission of reflectionless edge states have boosted intense research in classical systems such as photonics,<sup>[3–9]</sup> acoustics,<sup>[10–22]</sup> and mechanics.<sup>[23–26]</sup> Most recently, the concept of higher-order TIs (HOTIs),<sup>[27–33]</sup> which is a special class of TIs with unconventional bulk-boundary correspondence, was proposed to support the existence of the lower-dimensional boundary states. For example, in  $d$ -dimensional ( $d$ D) systems, a second-order TI (SOTI) has  $d$ D gapped bulk states,  $(d - 1)$ D gapped boundary states, and  $(d - 2)$ D gapless boundary states, which are 0D corner states

in 2D system. To date, HOTIs have been theoretically predicted and experimentally realized in elastics,<sup>[34,35]</sup> microwaves,<sup>[36]</sup> electric circuits,<sup>[37]</sup> photonics,<sup>[38–40]</sup> and acoustic systems.<sup>[41–46]</sup> In order to make HOTIs more attractive for real-world applications as in sound wave control, several hurdles must be overcome. For example, most of the reported results focus solely on a single frequency band, whose limitations ought to be overcome in order to provide a broadband response for topologically robust acoustics. Also, the above reported acoustic implementations have, for the most part, been implemented inside waveguides or were designed in an acoustically rigid enclosure, which hinders their capabilities from external insonification. Lastly, in terms of compactness, it is desired to utilize building blocks of the HOTI on a subwavelength scale in order to


confine sound in tight areas beyond the diffraction limit.

In this work, we design topologically protected acoustic corner states at deep subwavelength scales by constructing a perforated crystal, also known as holey metamaterials. The advantage in using holey metamaterials resides in their high levels of integration and miniaturization at scales much smaller than the sound wavelength. Without being pierced by holes, those metamaterials would not be able to sustain surface-confined wave propagation. With perforations on the other hand, externally incident radiation is able to bind to the structure in the form of “spoof” surface acoustic waves (SAWs), thus enabling sound energy confinement way beyond the classical diffraction limit.<sup>[47,48]</sup> In addition to breaking the diffraction limit for spoof SAWs, we demonstrate that a topological phase transition, which is derived from an extended 2D Zak phase, can be tuned by simply shrinking or expanding the distance among a group of holes within the unit cell. Beyond measuring corner states within multiple nontrivial bandgaps, the first-order resonance in particular displays the strongest topological sound energy confinement down to a feature size of  $\lambda/50$ . Lastly, we experimentally verify their resilience against defects and design a HOTI device for topological subwavelength imaging, which may be relevant for sound energy focusing and detection.

**Figure 1a** illustrates the schematic of deep-subwavelength acoustic SOTI under consideration, which is realized by a perforated rigid material whose holes are arranged in a square lattice. The perforation depth and the radii of holes are  $H = 12$  cm and  $r = 0.5$  cm, respectively. The lattice constant is  $a = 4.8$  cm. The center-to-center distance between the adjacent holes in the unit cell is defined as  $R$ , which is chosen to be  $R/a = 0.5$  for the

Z. Zhang, Dr. H. Long, C. Liu, C. Shao, Prof. Y. Cheng, Prof. X. Liu  
Department of Physics  
MOE Key Laboratory of Modern Acoustics  
Collaborative Innovation Center of Advanced Microstructures  
Nanjing University  
Nanjing 210093, China  
E-mail: chengying@nju.edu.cn; liuxiaojun@nju.edu.cn

Z. Zhang, Prof. J. Christensen  
Department of Physics  
Universidad Carlos III de Madrid  
ES-28916 Leganés, Madrid, Spain  
E-mail: johan.christensen@uc3m.es

 The ORCID identification number(s) for the author(s) of this article can be found under <https://doi.org/10.1002/adma.201904682>.

© 2019 The Authors. Published by WILEY-VCH Verlag GmbH & Co. KGaA, Weinheim. This is an open access article under the terms of the Creative Commons Attribution License, which permits use, distribution and reproduction in any medium, provided the original work is properly cited.

DOI: 10.1002/adma.201904682

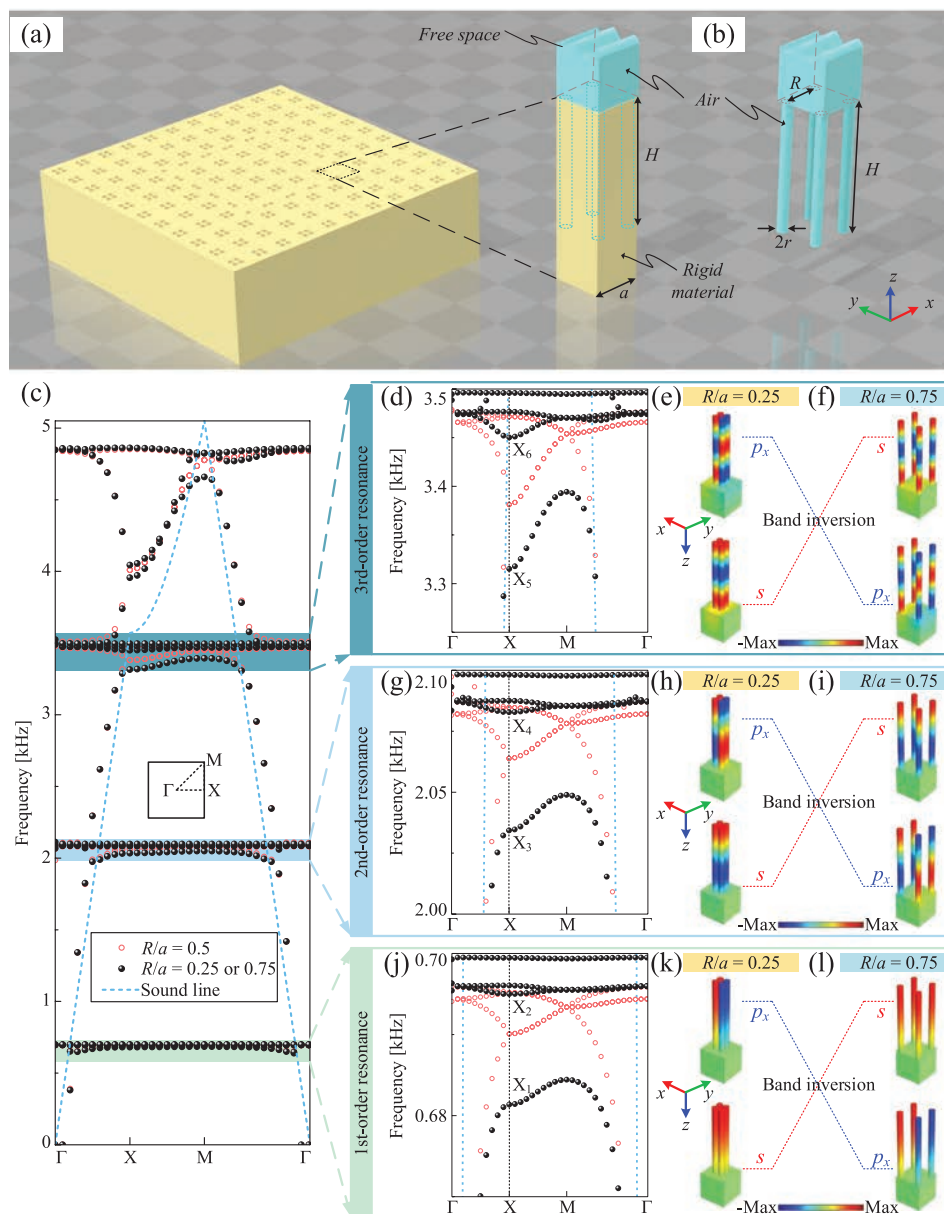


**Figure 1.** a) Schematic of the deep-subwavelength acoustic second-order topological insulator composed of a pierced hole square lattice. Inset: the unit cell containing four drilled holes. The yellow and cyan regions represent acoustic rigid material and background medium air, respectively. b) Corresponding air region of the unit cell. Free space is labeled with a wavy plane and extends infinitely along the  $z$ -direction. c) Dispersion relations of the ordinary PnC with  $R/a = 0.5$ , which is labeled by red circles, the shrunk PnC with  $R/a = 0.25$ , and the expanded PnC with  $R/a = 0.75$ , which is labeled by the black dots, respectively. The blue dashed curve represents the sound line and the inset shows the first Brillouin zone. d) Enlarged view of the band diagram comprising the third-order resonance. e, f) Band inversion between the trivial states of the shrunk unit cell  $R/a = 0.25$  (e) and the nontrivial states of the expanded unit cell  $R/a = 0.75$  (f). The rainbow colors represent the pressure distributions of the eigenstates  $X_5/X_6$  at the X point. g–i) Same as (d)–(f) but for the second-order resonance and j–l) for the first-order resonance.

regular square lattice (not shown here). Figure 1b illustrates the air domain of the unit cell in the simulations utilizing the finite-element software COMSOL Multiphysics. The wave-shaped top plane in the illustrations represents the infinite extension of free space that is set as plane wave radiation boundary conditions in the simulations. The velocity and mass density of air are  $c_0 = 343 \text{ m s}^{-1}$  and  $\rho_0 = 1.21 \text{ kg m}^{-3}$ , respectively. From the band diagrams in Figure 1c, the bands located around the first-, second-, and third-order resonance can be seen. Note that the propagation of the spoof SAWs confined to the surface of the

apertures can be ensured by the presence of these bands below the sound line. The sound line is the acoustic dispersion relationship in air background, which can be defined as  $f = |\mathbf{k}| \cdot c_0/2\pi$  with  $\mathbf{k}$  the wave vector along the boundary of the first Brillouin zone (BZ) and  $c_0$  the velocity of air. For a better view of the dispersion relation, the enlarged views of the band diagrams around the multiorder resonances are illustrated in Figure 1d, g, j. Taking the third-order resonance in Figure 1d as an example, the first two bands are degenerated along the XM direction with  $R/a = 0.5$ , which are labeled by red circles. The degeneracy is

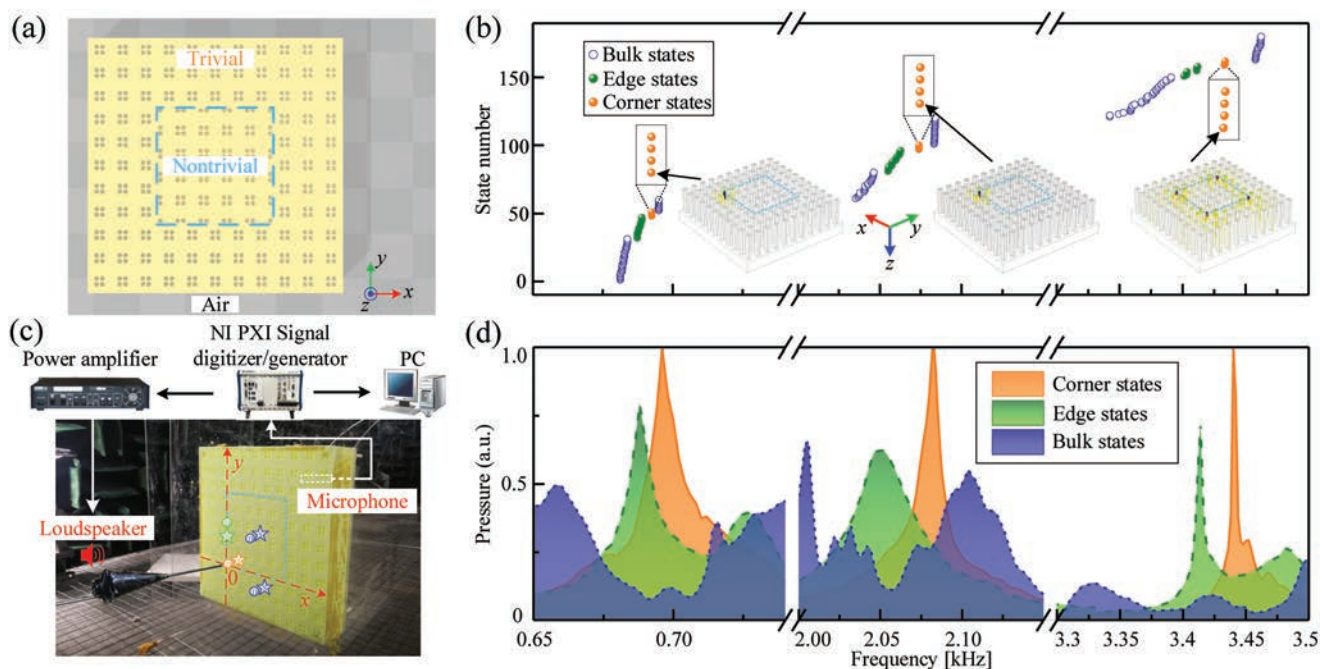


**Figure 2.** a) Schematic of the deep-subwavelength concentric square crystal which consists of a square nontrivial region surrounded by a trivial region whose interface is labeled by a cyan dashed frame. b) Calculated eigenfrequencies of the CSC near the first-, second- and third-order resonances, respectively. Insets: corresponding acoustic modes of the three corner states induced by different resonances. c) Photograph of a fabricated CSC sample. The blue, green, and orange colored stars represent the position of the point source and the dots are the position of the microphone when measuring the pressure spectra. d) Measured pressure spectra for bulk, edge, and corner states.

lifted to create a bandgap when introducing the perturbation such as shrinking the distance between the four holes in the unit cell to  $R/a = 0.25$  or expanding it to  $R/a = 0.75$ , shown by black dots in the corresponding band diagrams. Figure 1e further shows the acoustic modes  $X_5/X_6$  at the high symmetry point X where  $R/a = 0.25$ . Two points should be noted. i) The distributions of the pressure fields verify that the eigenmodes  $X_5/X_6$  are induced by the third-order resonance. ii) The profile of the lower eigenmode  $X_5$  is similar to the  $s$  orbit, which possesses an even parity (+). The profile of the upper eigenmode  $X_6$ , however, is similar to  $p_x$  orbit, which has an odd parity (-). We emphasize that the band diagrams are identical if the distance between the four holes in the unit cell is expanded to  $R/a = 0.75$ , however, the parities of the eigenmodes  $X_5/X_6$  will be inverted as shown in Figure 1f, where the profile of the lower eigenmode  $X_5$  has an odd parity (-) while the upper one has an even parity (+). Note that the bands/parities inversion can also be generated around the frequency ranges of the second- and first-order resonances, which are illustrated in Figure 1g–i, respectively, in detail.

We demonstrate that the band inversion signifies a topological phase transition, which can be characterized by a 2D Zak phase.<sup>[49,50]</sup> The Zak phase  $\mathbf{P}$  can be calculated by the parities at high symmetric points through<sup>[33,43,50,51]</sup>

$$P_i = \pi \left( \sum_n q_i^n \text{ modulo } 2 \right), \quad (-1)^{q_i^n} = \frac{\eta_n(X_i)}{\eta_n(\Gamma)}, \quad \text{with } (i = x, y) \quad (1)$$

in which  $\eta_n$  represents the parity ( $\pm$ ) of the  $n$ th band at the different high symmetric point and  $X_x/X_y$  denotes the X/Y point of the first BZ. We emphasize that  $\sum_1^n q^n$  in Equation (1) represents the sum of  $q$  from the first band to

the  $n$ th band, meaning all the bands below the targeted  $n$ th band. Due to the existence of the  $C_{4v}$  symmetry in the proposed structure, the  $x$ -direction Zak phase  $P_x$  is identical to the  $y$ -direction, i.e.,  $P_x = P_y$ . According to the parities at X point shown in Figure 1d–i and those at  $\Gamma$  point shown in Note S1, Supporting Information, the extended Zak phase is  $\mathbf{P} = (0, 0)$  when the distance  $R/a < 0.5$ , which means the structure is in the topological trivial phase. On the contrary, the Zak phase  $\mathbf{P} = (\pi, \pi)$  when  $R/a > 0.5$  demonstrates that the structure is in the topological nontrivial phase. Note that the presence of the topological edge state along  $x/y$  direction is guaranteed by the nonzero Zak phase  $P_y/P_x$  according to the bulk-edge correspondence.<sup>[8]</sup> We demonstrate that the nontrivial dipole moments in both directions form a quadruple tensor at the  $90^\circ$  terminated corner, which is a convergence of the interface polarization along both directions. Consequently, the corner state can be protected in a hierarchy of the bulk-edge and edge-corner correspondence which can be defined as a topological corner charge<sup>[40,43]</sup>

$$Q^{\text{corner}} = \frac{P_x P_y}{\pi^2} \quad (2)$$

From Equation (2), the topological corner charge  $Q^{\text{corner}} = 1$  ensures the existence of the topological corner states at the  $90^\circ$  terminated corner of the nontrivial region.

According to the above discussion, we construct a holey concentric square crystal (CSC) composed out of a  $5a \times 5a$  nontrivial region with  $R/a = 0.75$  enclosed by a trivial region with  $R/a = 0.25$  to observe the corner states. The thickness of the trivial region is  $3a$  as shown in Figure 2a. The calculated

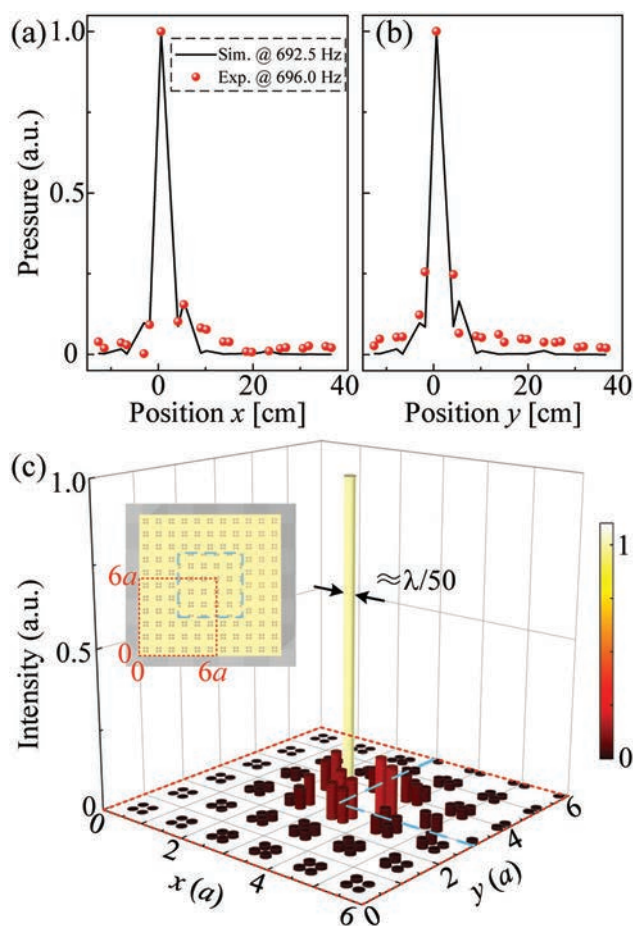


**Figure 3.** a,b) Simulated and experimentally measured spatial distributions of the sound pressure field for the corner state along the  $x$  direction (a) and  $y$  direction (b) as indicated by the red dashed lines in Figure 2c at the frequency of first-order resonance. c) Experimental sound-intensity fields of the corner state at  $f = 696$  Hz. Inset: the  $6a \times 6a$  measured region composed of  $12 \times 12$  holes is marked by a red dashed frame.

discrete eigenfrequencies near the three resonances are illustrated in Figure 2b. Note that in the topological bandgaps near each resonance, topological edge states and four degenerated corner states exist. From the acoustic profiles of the eigenmodes presented in the insets, topological corner states induced by different resonances can be clearly discerned, showing how the sound energy confines within the holes that are located at the corners. We emphasize that the eigenfrequencies of the corner states induced by the three resonances are 692.5, 2074.1, and 3433.7 Hz. As a result, the ratios between the lattice constant and the corresponding wavelength are  $a/\lambda = 0.097, 0.290,$  and  $0.481$ , respectively, which unequivocally shows that the holey CSC can sustain subwavelength corner states at three different frequencies in the audible range. We demonstrate that the corner states still can be obtained in a complementary configuration where a trivial structure is surrounded by a nontrivial one (Note S2, Supporting Information).

The holey CSC was constructed via 3D printing a thick epoxy resin plate by excluding voids to form the holes during the printing process. The mass density and the longitudinal velocity

of epoxy resin are  $\rho_e = 1050 \text{ kg m}^{-3}$  and  $c_e = 2200 \text{ m s}^{-1}$ , respectively. As a result, the epoxy resin can be treated as a rigid material due to its impedance  $Z_e = \rho_e c_e = 2.31 \times 10^6 \text{ kg m}^{-2} \text{ s}^{-1}$  which is much larger than the one of air  $Z_0 = \rho_0 c_0 = 415 \text{ kg m}^{-2} \text{ s}^{-1}$  (mass density  $\rho_0 = 1.21 \text{ kg m}^{-3}$  and velocity  $c_0 = 343 \text{ m s}^{-1}$ ). The sample, which is seen in Figure 2c, has been set up in an anechoic chamber and a point source is placed at the distance of 5 mm away from the surface of the sample to excite spoof SAW. The acoustic pressure amplitude is detected by a microphone from the back of the sample, i.e., the bottom of the holes. We measured the transmission spectra of the bulk, edge, and corner states as shown in Figure 2d. The placements of the source and the detecting microphones are labeled by colored letters “S” and “D” in Figure 2c. The transmission peaks of the corresponding edge and corner states can be clearly seen within the bandgaps of their complementary resonances. The transmission peaks of the topological corner states induced by the first-, second-, and third-order resonances appear at the frequencies 696, 2082, and 3440 Hz, respectively, which agree very well with the simulated results in Figure 2b.

Furthermore, in order to demonstrate the extreme confinement of the topological state bound to the corners, we measured the normalized pressure amplitude profile in each hole along the  $x$  and  $y$  directions with the left-bottom corner being the point of origin as indicated in Figure 2c. **Figure 3a,b** renders a good agreement between simulated and measured spatial maps along said directions, indicating the tight sound concentration at the origin. To visualize the full scope of the corner state concentration beyond the diffraction limit, we experimentally scan a square area, the red dashed frame in Figure 3c, in which we measure the normalized acoustic intensity at each hole bottom within this region. Our measurement results display an ultratight acoustic corner state at 696 Hz. Figure 3c verifies how the intensity peak centers within the square area and that this holey topological structure is capable of confining sound down to a diameter of  $d \approx \lambda/50$ . Additional simulations and discussion on the properties of the spoof SAWs are discussed carefully in Note S3, Supporting Information.

The hallmark and key manifestation of topological states is the robustness against defects. Hence, we demonstrate that the proposed deep-subwavelength SOTI displays remarkable resilience against bulk disorder over extended frequency band. To verify this experimentally, we introduce several disordered entities by concealing (inserting solid cylinders) random holes near the corners (purple dashed circles in **Figure 4a**) or slightly farther away from them (green dashed circles in **Figure 4a**). **Figure 4b–d** illustrates the measured transmission spectra of the topological corner states with and without the said two kinds of defects for comparison. After introducing the defects, the topological corner states remain within the three bandgaps with negligible frequency shifts, verifying an excellent durability of these deeply confined corner states. Furthermore, the influence of the defects introduced by changing the position or the size of the corner holes is discussed in Note S4, Supporting Information in detail, which also displays remarkable robustness of corner states against these defects.

Finally, we design an acoustic imaging device based on our SOTI and the associated topological corner states. As shown

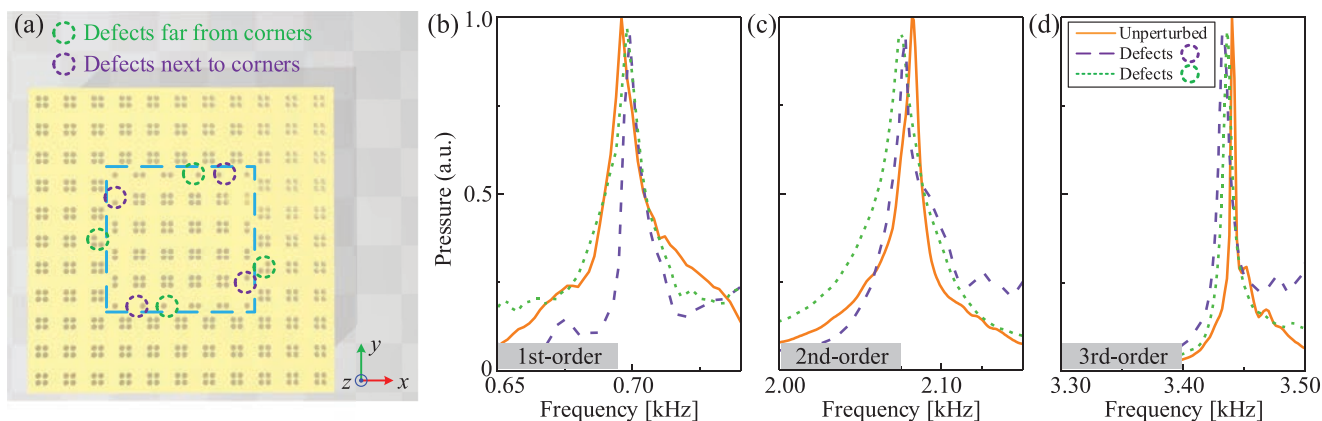


**Figure 4.** a) Introducing defects into the structure by inserting solid cylinders into four random holes next to the corners, which are labeled by purple circles, or by inserting solid cylinders into other four random holes a little farther away from the corners, which are labeled by green circles. The cyan dashed frame represents the interface between the trivial and nontrivial regions. b–d) Measured pressure spectra for the corner states of the unperturbed SOTI (orange solid curve), SOTI with defects near the corners (purple dashed curve), and the SOTI with defects farther away from the corners (green dotted curve), respectively, in three bandgaps.

in **Figure 5**, the programmable SOTI consists of two subwavelength digital elements of “0” and “1,” which correspond to the unit cells of the topological trivial state with the topological corner charge  $Q^{\text{corner}} = 0$  ( $R/a = 0.25$ ) and the topological nontrivial state with  $Q^{\text{corner}} = 1$  ( $R/a = 0.75$ ), respectively. Figure 5a illustrates a  $11 \times 11$  element array to image a heart-like acoustic profile. The emitting source with frequency  $f = 692.5$  Hz is placed near the surface of the programmable SOTI to excite the corner states of the first-order resonance. As we discussed

earlier, it is possible to excite corner states in complementary CSC configurations where the trivial and nontrivial regions are interchanged. The resulting difference is a slight frequency variation between the otherwise identical states (Note S2, Supporting Information). In order to program the SOTI to form a specific shape or letter, consequently a configuration is coded that contains simultaneous nontrivial–trivial interfaces and the exact opposite. Consequently, when a single-frequency sound signal is launched, one thus needs to bear in mind that

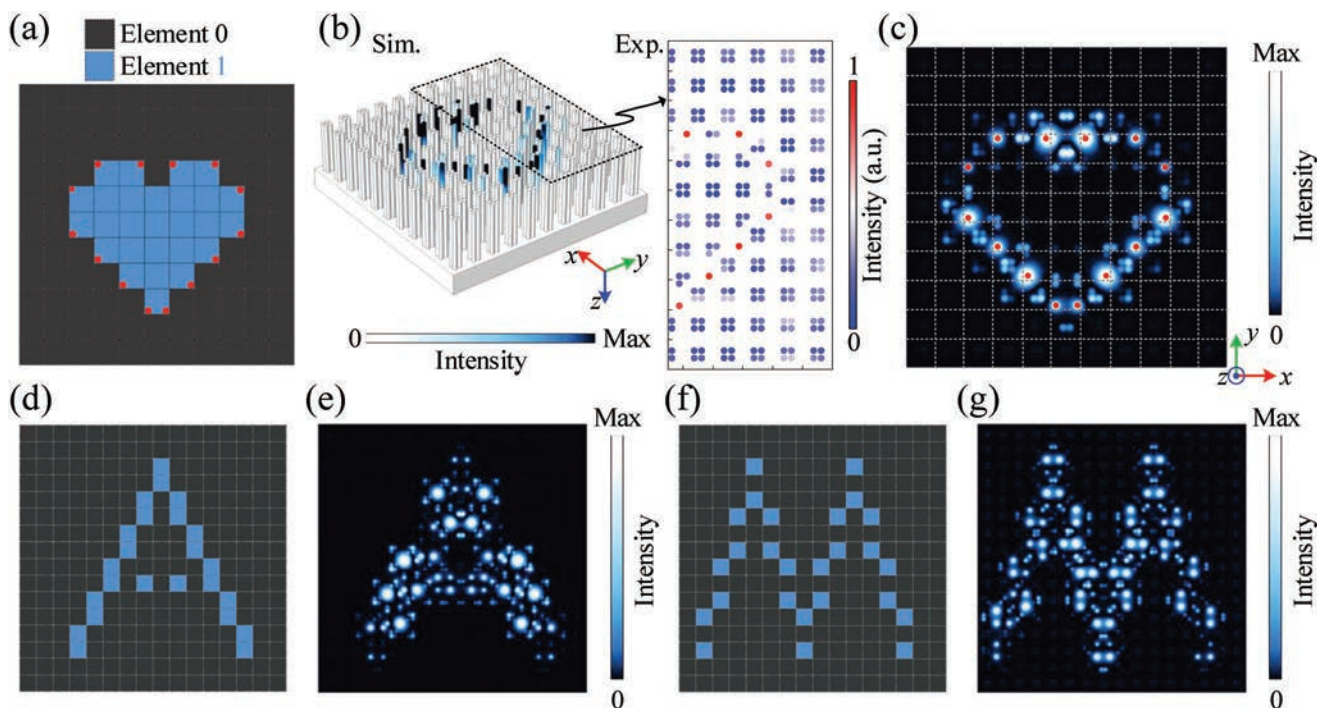


**Figure 5.** a) Programmable subwavelength SOTI imaging device composed of a heart-like nontrivial region (elements 1) surrounded by trivial region (elements 0). The red dots represent the corners that should be excited as the topological corner states. b) Simulated (left panel) and experimentally measured (right panel) distributions of the sound intensity fields for the heart-like image. c) Sound intensity distributions in the  $xy$ -plane at a distance of 0.1 mm above the holey CSC surface. The red dots represent the corners that should be excited. d) Coding arrays and e) sound intensity distributions on the cross section of the acoustic image for letter “A.” f, g) Same as (d) and (e), but for imaging letter “M.”

only specific corner states can be spectrally excited, which are labeled by red dots in Figure 5a at the frequency  $f = 692.5$  Hz. The simulated distribution of the sound intensity field is illustrated in Figure 5b, which renders the subwavelength heart-like image. The measured acoustic image is one half of the sample illustrated in the right panel of Figure 5b. The experimental data verify that most energy is confined at the corners whose positions are identical to the predicted ones labeled by red dotted corners in Figure 5a. The excellent agreement between the predicted and experimentally measured results confirms the validity of the acoustic imaging device based on the proposed deep-subwavelength SOTI. To emphasize that the imaging procedure is rooted in the coupling to spoof SAWs, we map the same image at a distance of 0.1 mm away from the structure surface into free space as seen in Figure 5c where the heart shape maintains its subwavelength features. One can observe that most of the energy is highly confined at the targeted corners labeled by red dots in Figure 5a and energy decays exponentially into the nontrivial and trivial regions. We emphasize that the corner states still exist and therefore topological acoustic imaging is still possible, even when the numbers of nontrivial cells are reduced to one single cell (Note S5, Supporting Information). As a result, imaging of different shapes can be tuned by coding the various holey array elements. For example, Figure 5d,f illustrates a  $16 \times 16$  element arrays of letters “A” and “M,” respectively. The corresponding sound intensity distributions across the  $xy$ -plane are shown in Figure 5e,g. Based on the above discussed frequency shift, fortunately, only marginal intensity variations of the corner states excitations of the acoustic imaging of characters “A” and “M” are seen as illustrated in Figure 5e,g. Hence, by programming the holey elements as desired, one is able to produce a broad variety of topologically robust deep-subwavelength images. We demonstrate that it is possible to conduct the programming with a given array. We propose a feasible experimental setup to achieve the real-time programming of SOTI in Note S6, Supporting Information. Beyond acoustic imaging, the proposed programmable SOTI may be also utilized for energy harvesting, which is discussed in Note S7, Supporting Information.

In conclusion, we have demonstrated the marriage of spoof surface acoustic waves and second-order topological insulators supporting extremely confined subwavelength corner states. The presence of the topological corner state is ensured by the hierarchical combination of the bulk-edge and edge-corner correspondences. Not only did we experimentally explore those topologically robust corner states across three different frequency bands, we additionally measured sound intensity concentration in the long wavelength regime comprising highly confined corner states of diameter 50 times smaller than the sound wavelength. We foresee that our findings may provide the unique possibility to advance the design of acoustic functional devices based on deep subwavelength topologically robust and programmable acoustic insulators relevant for imaging and energy harvesting.

## Experimental Section

The proposed SOTI was precision-fabricated using epoxy resin via 3D printing. The fabricated sample in Figure 2c consisted of 484 holes of

radius 0.5 cm and depths 12 cm. The sample was set up vertically in an anechoic chamber. The experiments were conducted by one loudspeaker with gradient pipes to generate a point-like sound source, which was placed near the surface of the holes at a distance of 0.5 cm. Local pressure fields were measured by inserting the condensed microphones (GRAS type 40PH) into the bottom of designated holes from the backside of the SOTI. The outputs of the microphones were acquired by a digitizer (NI PXI-4498), and processed by LabVIEW software. A frequency scan of the transmission spectra in Figures 2d and 4b–d was performed with an increment of 0.001 kHz.

## Supporting Information

Supporting Information is available from the Wiley Online Library or from the author.

## Acknowledgements

Z.Z. and H.L. contributed equally to this work. This work was supported by the National Key R&D Program of China (2017YFA0303702), NSFC (11922407, 11834008, 11874215, 11674172, and 11574148), Jiangsu Provincial NSF (BK20160018), the Fundamental Research Funds for the Central Universities (020414380001), and Nanjing University Innovation and Creative Program for Ph.D. candidate (CXCY17-11). Z.Z. acknowledges the support from the China Scholarship Council. J.C. acknowledges the support from the European Research Council (ERC) through the Starting Grant 714577 PHONOMETA and from the MINECO through a Ramón y Cajal grant (Grant No. RYC-2015-17156).

## Conflict of Interest

The authors declare no conflict of interest.

## Keywords

deep-subwavelength acoustic imaging, phononic crystals, second-order topological insulators, spoof surface acoustic waves, topological corner states

Received: July 21, 2019  
Revised: September 14, 2019  
Published online: October 25, 2019

- [1] M. Z. Hasan, C. L. Kane, *Rev. Mod. Phys.* **2010**, *82*, 3045.
- [2] X. L. Qi, S. C. Zhang, *Rev. Mod. Phys.* **2011**, *83*, 1057.
- [3] F. Haldane, S. Raghu, *Phys. Rev. Lett.* **2008**, *100*, 013904.
- [4] Z. Wang, Y. Chong, J. D. Joannopoulos, M. Soljačić, *Phys. Rev. Lett.* **2008**, *100*, 013905.
- [5] A. B. Khanikaev, S. H. Mousavi, W. K. Tse, M. Kargarian, A. H. MacDonald, G. Shvets, *Nat. Mater.* **2013**, *12*, 233.
- [6] L. Lu, J. D. Joannopoulos, M. Soljačić, *Nat. Photonics* **2014**, *8*, 821.
- [7] A. B. Khanikaev, G. Shvets, *Nat. Photonics* **2017**, *11*, 763.
- [8] F. Liu, H. Y. Deng, K. Wakabayashi, *Phys. Rev. B* **2018**, *97*, 035442.
- [9] T. Ozawa, H. M. Price, A. Amo, N. Goldman, M. Hafezi, L. Lu, M. C. Rechtsman, D. Schuster, J. Simon, O. Zilberberg, I. Carusotto, *Rev. Mod. Phys.* **2019**, *91*, 015006.
- [10] Z. Yang, F. Gao, X. Shi, X. Lin, Z. Gao, Y. Chong, B. Zhang, *Phys. Rev. Lett.* **2015**, *114*, 114301.
- [11] A. B. Khanikaev, R. Fleury, S. H. Mousavi, A. Alu, *Nat. Commun.* **2015**, *6*, 8260.
- [12] M. Xiao, W. J. Chen, W. Y. He, C. T. Chan, *Nat. Phys.* **2015**, *11*, 920.

- [13] R. Fleury, A. B. Khanikaev, A. Alu, *Nat. Commun.* **2016**, 7, 11744.
- [14] Z. Zhang, Q. Wei, Y. Cheng, T. Zhang, D. Wu, X. Liu, *Phys. Rev. Lett.* **2017**, 118, 084303.
- [15] Z. Zhang, Y. Tian, Y. Cheng, X. Liu, J. Christensen, *Phys. Rev. B* **2017**, 96, 241306.
- [16] Q. Wei, Y. Tian, S. Y. Zuo, Y. Cheng, X. J. Liu, *Phys. Rev. B* **2017**, 95, 094305.
- [17] J. Lu, C. Qiu, L. Ye, X. Fan, M. Ke, F. Zhang, Z. Liu, *Nat. Phys.* **2017**, 13, 369.
- [18] Y. Deng, H. Ge, Y. Tian, M. Lu, Y. Jing, *Phys. Rev. B* **2017**, 96, 184305.
- [19] Z. Zhang, Y. Tian, Y. Cheng, Q. Wei, X. Liu, J. Christensen, *Phys. Rev. Appl.* **2018**, 9, 034032.
- [20] Z. Zhang, Y. Tian, Y. Wang, S. Gao, Y. Cheng, X. Liu, J. Christensen, *Adv. Mater.* **2018**, 30, 1803229.
- [21] H. He, C. Qiu, L. Ye, X. Cai, X. Fan, M. Ke, F. Zhang, Z. Liu, *Nature* **2018**, 560, 61.
- [22] X. Zhang, M. Xiao, Y. Cheng, M. H. Lu, J. Christensen, *Commun. Phys.* **2018**, 1, 97.
- [23] R. Süsstrunk, S. D. Huber, *Science* **2015**, 349, 47.
- [24] S. H. Mousavi, A. B. Khanikaev, Z. Wang, *Nat. Commun.* **2015**, 6, 8682.
- [25] M. Miniaci, R. Pal, B. Morvan, M. Ruzzene, *Phys. Rev. X* **2018**, 8, 031074.
- [26] Y. Chen, X. Liu, G. Hu, *J. Mech. Phys. Solids* **2019**, 122, 54.
- [27] W. A. Benalcazar, B. A. Bernevig, T. L. Hughes, *Science* **2017**, 357, 61.
- [28] J. Langbehn, Y. Peng, L. Trifunovic, F. von Oppen, P. W. Brouwer, *Phys. Rev. Lett.* **2017**, 119, 246401.
- [29] Z. Song, Z. Fang, C. Fang, *Phys. Rev. Lett.* **2017**, 119, 246402.
- [30] W. A. Benalcazar, B. A. Bernevig, T. L. Hughes, *Phys. Rev. B* **2017**, 96, 245115.
- [31] M. Ezawa, *Phys. Rev. Lett.* **2018**, 120, 026801.
- [32] F. Schindler, A. M. Cook, M. G. Vergniory, Z. Wang, S. S. Parkin, B. A. Bernevig, T. Neupert, *Sci. Adv.* **2018**, 4, eaat0346.
- [33] F. Liu, H. Y. Deng, K. Wakabayashi, *Phys. Rev. Lett.* **2019**, 122, 086804.
- [34] M. Serra-Garcia, V. Peri, R. Süsstrunk, O. R. Bilal, T. Larsen, L. G. Villanueva, S. D. Huber, *Nature* **2018**, 555, 342.
- [35] H. Fan, B. Xia, L. Tong, S. Zheng, D. Yu, *Phys. Rev. Lett.* **2019**, 122, 204301.
- [36] C. W. Peterson, W. A. Benalcazar, T. L. Hughes, G. Bahl, *Nature* **2018**, 555, 346.
- [37] S. Imhof, C. Berger, F. Bayer, J. Brehm, L. W. Molenkamp, T. Kiessling, F. Schindler, C. H. Lee, M. Greiter, T. Neupert, R. Thomale, *Nat. Phys.* **2018**, 14, 925.
- [38] B. Y. Xie, H. F. Wang, H. X. Wang, X. Y. Zhu, J. H. Jiang, M. H. Lu, Y. F. Chen, *Phys. Rev. B* **2018**, 98, 205147.
- [39] X. D. Chen, W. M. Deng, F. L. Shi, F. L. Zhao, M. Chen, J. W. Dong, *Phys. Rev. Lett.* **2019**, 122, 233902.
- [40] Y. Ota, F. Liu, R. Katsumi, K. Watanabe, K. Wakabayashi, Y. Arakawa, S. Iwamoto, *Optica* **2019**, 6, 786.
- [41] H. Xue, Y. Yang, F. Gao, Y. Chong, B. Zhang, *Nat. Mater.* **2019**, 18, 108.
- [42] X. Ni, M. Weiner, A. Alù, A. B. Khanikaev, *Nat. Mater.* **2019**, 18, 113.
- [43] Z. Zhang, M. R. López, Y. Cheng, X. Liu, J. Christensen, *Phys. Rev. Lett.* **2019**, 122, 195501.
- [44] X. Zhang, H. X. Wang, Z. K. Lin, Y. Tian, B. Xie, M. H. Lu, Y. F. Chen, J. H. Jiang, *Nat. Phys.* **2019**, 15, 582.
- [45] H. Xue, Y. Yang, G. Liu, F. Gao, Y. Chong, B. Zhang, *Phys. Rev. Lett.* **2019**, 122, 244301.
- [46] M. Weiner, X. Ni, M. Li, A. Alù, A. B. Khanikaev, *preprint arXiv:1903.00428* **2019**.
- [47] J. Christensen, A. Fernandez-Dominguez, F. de Leon-Perez, L. Martin-Moreno, F. Garcia-Vidal, *Nat. Phys.* **2007**, 3, 851.
- [48] J. Zhu, J. Christensen, J. Jung, L. Martin-Moreno, X. Yin, L. Fok, X. Zhang, F. Garcia-Vidal, *Nat. Phys.* **2011**, 7, 52.
- [49] J. Zak, *Phys. Rev. Lett.* **1989**, 62, 2747.
- [50] C. Fang, M. J. Gilbert, B. A. Bernevig, *Phys. Rev. B* **2012**, 86, 115112.
- [51] F. Liu, K. Wakabayashi, *Phys. Rev. Lett.* **2017**, 118, 076803.